Optics Communications 448 (2019) 116–123

Contents lists available at ScienceDirect

Optics Communications

journal homepage: www.elsevier.com/locate/optcom

Rayleigh and sodium lidar system incorporating time-division and wavelength-division multiplexing

Ju Ma [a], Mingjia Shangguan [a], Haiyun Xia [a,b,*], Xin Fang [a,c,*], Xianghui Xue [a,c,d], Xiankang Dou [a,e]

[a] CAS Key Laboratory of Geospace Environment, University of Science and Technology of China, Hefei, 230026, China
[b] Glory China Institute of Lidar Technology, Shanghai, 201315, China
[c] CAS Center for Excellence in Comparative Planetology, Hefei, 230026, China
[d] Mengcheng National Geophysical Observatory, School of Earth and Space Sciences, University of Science & Technology of China, Hefei, 230026, China
[e] Wuhan University, Wuhan 430072, China

ARTICLE INFO

Keywords:
Rayleigh lidar
Sodium resonance lidar
Mesosphere region

ABSTRACT

In this study, we report a Rayleigh and sodium lidar system, which was recently upgraded at the University of Science and Technology of China (USTC) in Hefei, China (31.5 °N, 117 °E). The lidar system features high temporal and vertical resolutions, a high signal-to-noise ratio (SNR) and mobility. Using the time-division and wavelength-division multiplexing methods, only one piece of photomultiplier tube is used in the optical receiver, which makes the system compact and robust. Wideband filtering and narrowband filtering are both used in the lidar system to obtain high SNR data under city lights. The lidar system was established on 24 September 2016 and has run stably for 2 years. Meteor trail events that lasted for only a few seconds were extracted from the high resolution, high SNR observational data. The sodium observational data in 2017 were fitted annually and semiannually, and the results were similar to those obtained in previous studies. The monthly average atmospheric temperature showed semiannual variations. Stratospheric aerosols were observed for two consecutive days during the observations.

1. Introduction

The middle and upper atmosphere is closely related to the human living environment. The stratosphere, mesosphere and lower thermosphere regions are affected not only by solar activity but also by the weather and climate of the Earth [1,2]. An increasing number of scholars have focused on the coupling process between the middle and upper atmospheres [3,4]. Thus, high resolutions, high SNR and long-term stable observational data are necessary to better understand the complex dynamics and chemical processes occurring in the stratosphere, mesosphere and lower thermosphere regions.

Atmospheric temperature and density in the stratosphere and mesosphere can be obtained by detecting the Rayleigh scattering signal [5–9]. However, the Rayleigh scattering signal is extremely weak in the region above 70 km, so Rayleigh lidar cannot easily obtain atmospheric data. There have been some efforts recently from the Rayleigh lidar groups to extend their data coverage into upper mesosphere [10,11] by increasing the power aperture product and new data analysis algorithm. The deposition of materials of extraterrestrial origin into the upper atmosphere results in layers of metal atoms or ions, mainly in the mesosphere and lower thermosphere (MLT) region, which ranges from 80 to 105 km. These metal particles have a scattering fluorescence property, which makes metal atoms good tracers of middle and upper atmosphere activities [12,13]. Sodium lidar can obtain the sodium atom density in the MLT region by emitting a laser with a sodium resonance wavelength (589.158 nm) and receiving the subsequent backscattered echo signal [14–18]. Sodium lidar observational data were used to study the chemical and dynamic processes in the MLT region, such as seasonal variations in the sodium layer [19–21], sporadic sodium layer [22–27], thermospheric-enhanced sodium layers [28–32], meteor trails [33,34], and gravity waves [35–37].

There were some lidar systems which can detect both atmospheric data and sodium data. The Rayleigh/Mie/Raman lidar and the sodium lidar at the ALOMAR Observatory (69°N, 16°E) in Northern Norway co-observed for more than 40 h during a joint campaign in January 2009 [38], collecting wind measurement data in the middle atmosphere from 30 to 110 km. These lidars shared a receiving telescope, and each lidar's signal detection and acquisition system was independent of each other. The Deep Propagating Gravity Wave Experiment (DEEPWAVE) took place from May to July 2014 using airborne Rayleigh and sodium lidar, providing measurements from the Earth's surface to 100 km [39]. The Rayleigh lidar was used to measure atmospheric density and temperature from ~20 to 60 km, and the sodium resonance lidar was used to measure sodium densities and temperatures from ~75 to 100 km.

* Corresponding authors at: CAS Key Laboratory of Geospace Environment, University of Science and Technology of China, Hefei, 230026, China.
E-mail addresses: hsia@ustc.edu.cn (H. Xia), xinf@ustc.edu.cn (X. Fang).

https://doi.org/10.1016/j.optcom.2019.05.010
Received 22 March 2019; Received in revised form 6 May 2019; Accepted 7 May 2019
Available online 11 May 2019
0030-4018/

Table 1
System parameters of the USTC Rayleigh-Sodium lidar.

Transmitter	Channel	
Laser	**Rayleigh**	**Sodium**
Wavelength (nm)	532	589
Pulse power (mJ)	500	60
Divergence (mrad)	0.5	0.5
Linewidth (cm^{-1})	1 (unseeded)	0.03 (dual grating)
Pulse width (ns)	6	5
Repetition (Hz)	50	50
Beam expander		
Magnification ratio	7	10
Beam divergence (μrad)	71.4	50.0
Receiver	Value	
Telescope	Cassegrain telescope	
Diameter (mm)	1000	
FOV (μrad)	125	
Chopper rotate rate (rpm)	3000	
Optical filter 1 & 2		
Bandpass (nm)	0.1	

However, prior lidar systems required multiple sets of lidar systems to work together to complete detections, resulting in high system complexity and high manufacturing costs. Using the time-division and wavelength-division multiplexing method, the USTC Rayleigh and sodium lidar uses dual channel acquisition of a single photomultiplier tube (PMT), making the system compact and robust.

In this paper, we discuss the USTC Rayleigh and sodium lidar system, which was recently upgraded in Hefei, China (31.5°N, 117°E). A detailed description of the overall structure of the lidar system and the wavelength-division multiplexing receiving system will be outlined in Section 2. In Section 3, the observational data results and analysis are provided. The conclusions are presented in Section 4.

2. Lidar system

In this lidar system, the Rayleigh channel can detect Rayleigh scatting signals ranging from 30–70 km to obtain atmospheric temperature and density, while the sodium channel can detect sodium resonance fluorescence scattering signals to obtain sodium densities ranging from 80–105 km. Using the time-division and wavelength-division multiplexing method, only one piece of PMT is used in the optical receiver, making the system compact and robust. There are no differences in signal amplification gain, photoelectric conversion efficiency, data acquisition threshold, and so on between the two channels, which simplifies the data fusion process. Wideband filtering and narrowband filtering are both used in the lidar system to obtain high SNR data under city lights. The lidar system was established on 24 September 2016 and has run stably for 2 years. From the data that have been collected, the system has an excellent resolution and SNR. The entire lidar system is located in a square-shaped cabin, as shown in Fig. 1, which makes the lidar system mobile.

The lidar system is mainly composed of four parts: transmitter unit, lock unit, receiver unit and control unit, as shown in Fig. 2. Table 1 lists the parameters of the lidar system.

2.1. Transmitter unit

The lidar transmitter consists of an Nd:YAG laser (Continuum Powerlite DLS 9050), an optical switcher (Newport XPS motor control driver and Newport XMS-100), a dye laser (Continuum VISTA) and a laser emission platform (Newport 605-4, Newport TRA12CC). The Rayleigh channel and sodium channel are controlled by the optical switcher device for time-division acquisition. When the Rayleigh channel operates, a 1064 nm laser generated by the Nd:YAG laser resonant cavity oscillation is amplified and multiplied by a Second Harmonic Generation (SHG) crystal to produce a 532 nm laser with a pulse energy of 500 mJ and a pulse repetition rate of 50 Hz. When the sodium channel operates, the transmitter is a tunable dye laser with a wavelength of 589 nm, a pulse energy of 60 mJ and a pulse repetition rate of 50 Hz pumped by the 532 nm Nd:YAG laser. Then, the 532 nm and 589 nm lasers are expanded by the beam expanders and vertically emitted into the sky by the mirrors on the laser emission platform. After

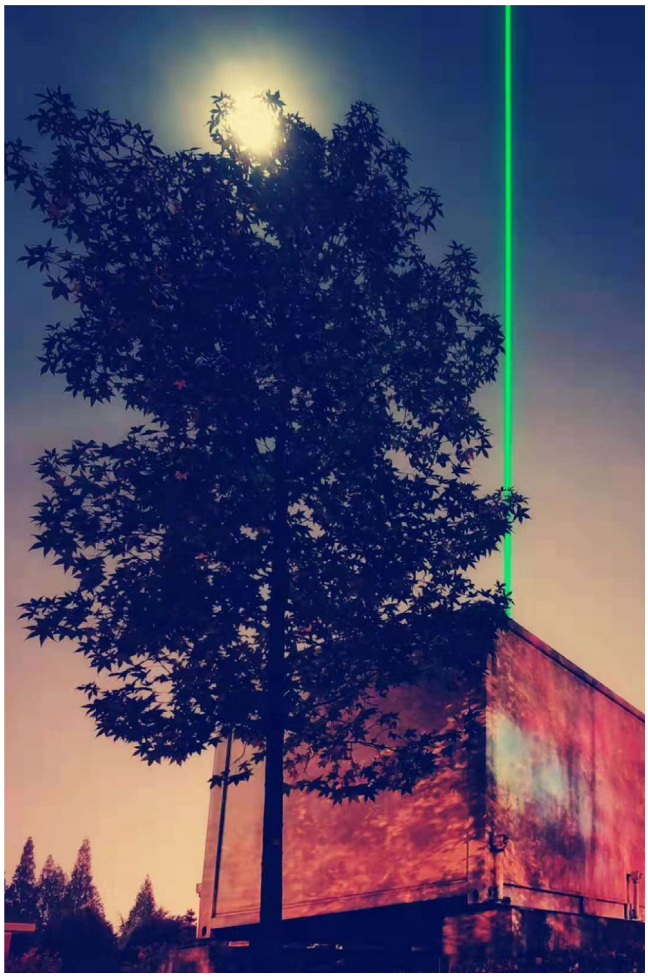

Fig. 1. Photograph of the Rayleigh and sodium lidar system.

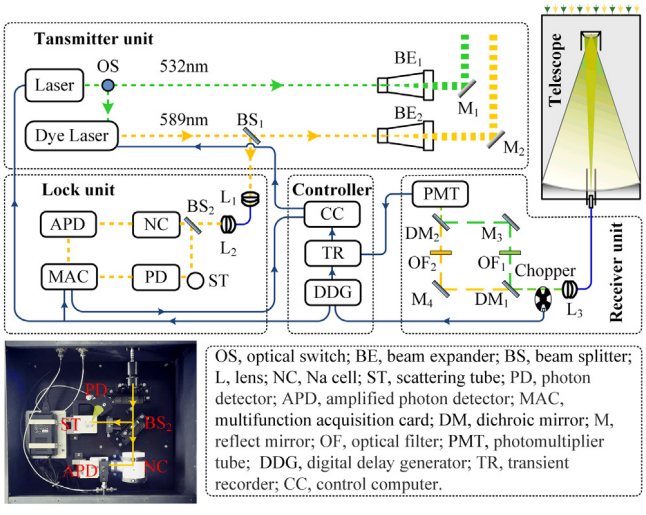

Fig. 2. Schematic diagram of the lidar system.

the beams is expanded, the actual divergence angles of the emitted beams are 71.4 μrad and 50.0 μrad for Rayleigh channel and sodium channel, respectively, which are small enough to ensure that the lidar overlap factor is 1. The emission angle of the beams can be fine-tuned by the Newport motor (Newport TRA12CC) to coincide with the optical axis of the telescope to achieve the highest SNR [40].

2.2. Lock unit

Since the wavelength of the dye laser output beam is not accurate, it needs to be calibrated by a wavelength lock system [41]. At first, the output beam is split into the lock system through BS_1, whose splitting ratio is 1:99 (R:T). Then, the laser beam is further split into two beams by BS_2, whose splitting ratio is 10:90 (R:T). The reflected beam is directed toward the scattering tube and the transmissive beam enters the sodium cell. Light scattered from the scattering tube is received by the photon detector (PD, ET-2030) to obtain the reference beam intensity. The saturation fluorescence emitted from the sodium cell is detected by the amplified photon detector (APD, PDA36A-EC) and recorded by the multifunction acquisition card (MAC, SRS SR250) to obtain the saturation fluorescence intensity. The relative saturation fluorescence intensity is equal to the ratio of saturated fluorescence intensity to reference intensity, which is not affected by the laser energy fluctuations. Then, a scan is performed to find the wavelength corresponding to the maximum relative saturation fluorescence intensity, which is at the sodium D_{2a} peak (589.158 nm). Then, the emitting laser wavelength is locked to the D_{2a} peak to achieve the best backscattering signals.

2.3. Receiver unit

The lidar receiver is composed of a receiving telescope, a chopper wheel system and a wavelength-division multiplexing receiving system.

The receiving telescope is a Cassegrain receiving telescope with a diameter of 1 meter. The receiving field of view of the telescope is 125 μrad. The main mirror is a paraboloid mirror, and the sub mirror is a hyperboloid mirror. Both the primary and secondary mirrors are coated with a dielectric film to accommodate the dual channel reception of 532 nm and 589 nm wavelength signals. The backscattered signal is collected by the receiving telescope and then coupled into the fiber through the fiber optic mount (Thorlabs Cage System), and the other end is close enough to the chopper wheel system.

Since the strong backscattering signals at low altitudes may damage the PMT, a chopper wheel with a diameter of 200 mm that rotates at a rate of 6000 rpm is set to block the low altitude signals [40,42]. The timing signals of the chopper wheel will be transmitted to the timing control system by a photoelectric switch and corresponding circuit.

Then, the processed backscattered signals enter the wavelength-division multiplexing receiving system. The wavelength-division multiplexing receiving system can divide the backscattered signals into 532 nm signals and 589 nm signals and separately perform filtering processing and then introduce the signals into the same PMT. The wavelength-division multiplexing receiving system consists of dichroic mirrors (DM_1 & DM_2, DMLP567), optical filters (OF_1 & OF_2), reflect mirrors (M_3 & M_4) and the PMT. The transmission and reflectance parameters of the dichroic mirrors are shown in Fig. 3. The backscattered signals are divided by the DM_1 into Rayleigh signals and sodium fluorescence signals. Rayleigh signals will be reflected by the DM_1 and filtered by the OF_1; then, the Rayleigh signals will be reflected by the M_3 and DM_2 and finally coupled into the PMT. The sodium fluorescence signals will be transmitted through the DM_1 and reflected by the M_4, and then, the sodium fluorescence signals will be filtered by the OF_2, transmitted through the DM_2 and finally coupled into the PMT. Wideband filtering (dichroic mirrors) and narrowband filtering (optical filters) are both used in the lidar system to obtain high SNR data under city lights. Since the Rayleigh signals generated by the 532 nm wavelength laser and the sodium resonance fluorescent signals generated by the 589 nm wavelength laser are both in the visible wavelength range, the photoelectric conversion of the two wavelength signals can be simultaneously performed using the same PMT.

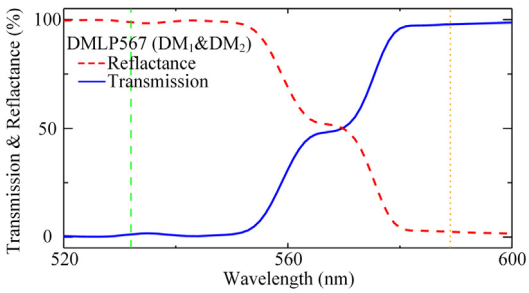

Fig. 3. The transmission and reflectance parameters of the dichroic mirror DMLP567. The blue solid line and red dashed line represent the transmission and reflectance, respectively. The green dashed line and orange dotted line represent the wavelengths of 532 nm and 589 nm, respectively.

The fiber used in the system is a large-diameter multimode fiber with an inner diameter of 1.5 mm. The optical fiber, the collimator and the coupling mirror are used to transmit, collimate and focus the dual channel signals with two different divergence angles. Thus, the effective diameter of the PMT used in this system is 5 mm, which is sufficiently large for a PMT to detect signals with two different divergence angles.

2.4. Control unit

Optical signals are converted into electrical signals by the PMT and then enter the transient recorder (Licel TR-20). The transient recorder samples signals according to the transistor logic (TTL) signals generated from the digital delay generator (DDG, SRS DG645) and the set sampling interval and quantity. The collected data will be stored in the control computer.

The timing control system plays an important role in the entire acquisition process, which determines the timing of the entire system and ensures that the system operates in the correct order. The DDG is mainly used for timing control, but the entire timing control system requires the coordination of many other devices: the optical chopper, the 9050 laser, the control computer and the transient recorder. The timing diagram is shown in Fig. 4. The timing signals of the optical chopper will be used as a master clock for the entire lidar system. The chopper is divided into 4 lobes and rotates at a frequency of 50 Hz, thus outputting a 200 Hz transistor-TTL signal called an optical chopper signal (OCS) to enter the DDG. The digital delay generator signal (DDGS) is triggered once every four input TTL pulses (rising edge), identical to a trigger with a frequency of 50 Hz. The flash lamp signal (FLS) is used to trigger a pulsed Nd:YAG flash lamp with 1825 μs and 1765 μs delays from DDGS for the sodium channel and Rayleigh channel, respectively. These delays compensate for the 180°out-of-phase between the gate opening and the optical chopper TTL rising edge, the opening transition time, and the pulsed YAG Q-switch delay from the flash lamp. The Q-switch signal (QSS) has a 294 μs delay from FLS, which is used to trigger the transient recorder. The chopper fully open altitudes are 28 km and 22 km for the Rayleigh channel and sodium channel, respectively.

After the acquisition of one channel is completed, the control computer will issue a channel switch command to the optical switcher and DDG and then begin the acquisition of the next channel. The switch interval is 4 min.

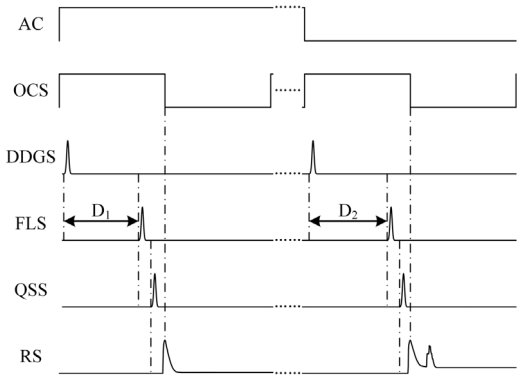

Fig. 4. Timing diagram of the USTC Rayleigh and sodium multichannel lidar. AC: acquisition channel, 1 refers to the Rayleigh channel, 0 refers to the sodium channel, and $T = 8$ min, which means the switch interval is 4 min; OCS: optical chopper signal, 1 refers to closing, 0 refers to opening, and f=200 Hz; DDGS: digital delay generator signal and f = 50 Hz; FLS: flash lamp signal, D_1 = 1765 μs, and D_2 = 1825 μs; QSS: Q-switch signal, delay with FL for 294 μs, pulse width = 100 μs, and f = 50 Hz; RS: raw signal, chopper fully open altitudes are 28 km for the Rayleigh channel and 22 km for the sodium channel.

3. Observational data and analysis

3.1. Dual channel observation

In the actual observation, the dual channel timing switch observational method is adopted, which has a switch interval of 4 min. The temporal and vertical resolutions of the Rayleigh channel are 30 s and 90 m, respectively. The temporal and vertical resolutions of the sodium channel are 2 s and 90 m, respectively. The USTC Rayleigh and sodium lidar have run stably for 2 years since 24 September 2016. The actual observation days exceeded 140 days, and more than 1800 h of observational data were collected. In the case of good weather, the Rayleigh signals can invert the atmospheric temperature and density up to over 70 km, and the SNR of the sodium signals can be stable over 60 (90 m, 240 s, $SNR = \frac{Na_{ave} - Bk_{ave}}{\sqrt{Na_{ave}}}$). Raw photon counts are shown in Fig. 5. The average SNR of the old lidar system observation sodium signals in November 2014 was 15.46, while the average SNR of the upgraded lidar system observation sodium signals in November 2017 was over 61.08.

The atmospheric temperature, density and sodium density observed on 20 July 2017 are shown in Fig. 6. As shown in Fig. 6a and 6b, using the Rayleigh scattering signal, the density and temperature can be obtained up to 80 km and 70 km, respectively. The sodium density can be obtained between ~80 and 105 km, and an obvious sporadic sodium layer occurred from 22:41 LT, as shown in Fig. 6c.

3.2. Meteor trail observations

As meteoroids (larger than 10 μg) enter the upper atmosphere at high speeds (11–72 km s^{-1}), they are evaporated by frictional heating and form spatially well-defined trails of meteoroid debris. When meteoroid debris passes through the lidar field of view, there will be a narrow width and short duration sodium density peak superimposed on the background sodium layer on the sodium layer density profile because of the sudden increase in sodium density. Most of the meteoroid debris trails last only a few seconds (1–3 s) within the range of the laser beam due to the effect of the wind field [33,43–46]. The USTC Rayleigh and sodium lidar have high temporal and vertical resolutions and a high SNR, which is adequate for the extraction of meteor trails with a time scale of several seconds. To extract meteor trials from the large observation dataset, we followed a method similar to that used in previous studies [34,47]:

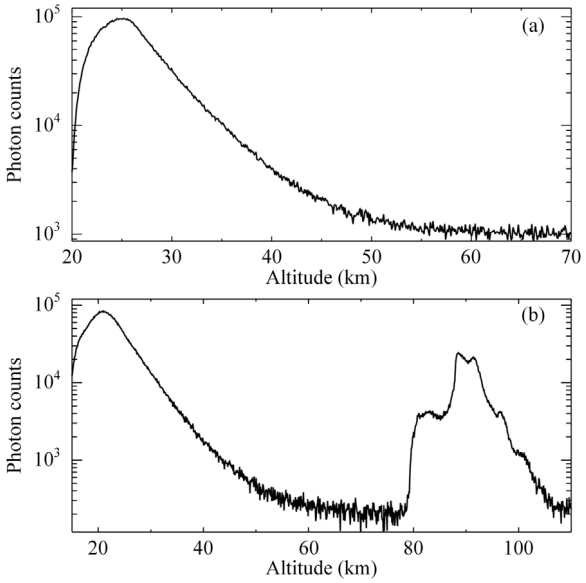

Fig. 5. Raw signals in the Rayleigh channel (a) and sodium channel (b). The temporal and vertical resolutions of the sodium channel are 240 s and 90 m, respectively.

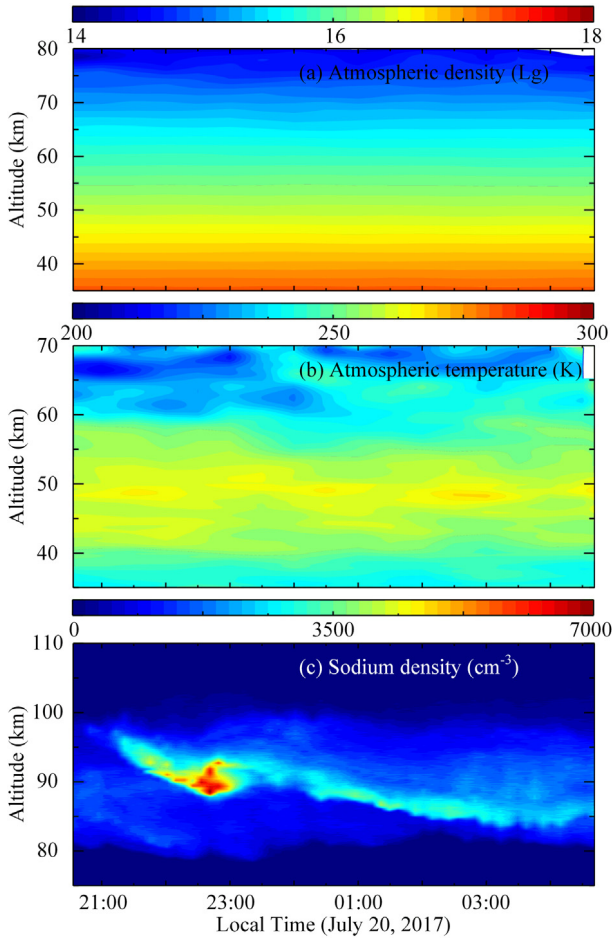

Fig. 6. Atmospheric density (a), temperature (b) and sodium density (c) observed over Hefei in on July 2017.

The photon count in a single altitude channel (0.9 km) and a single time bin (2 s) is considered to follow a Poisson distribution. The mean

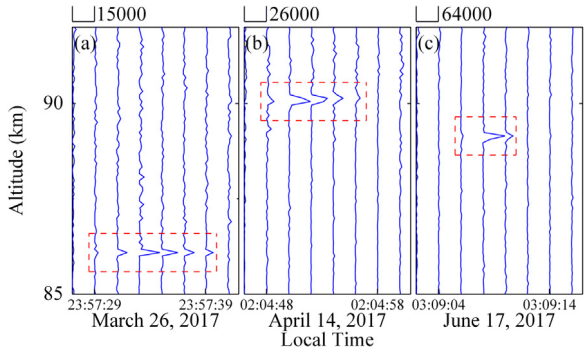

Fig. 7. Sodium density profiles of meteor trail events that occurred on 26 March 2017 (a), 15 April 2017 (b) and 18 June 2017 (c), respectively. The red dashed lines show regional times and heights of meteor trail events. The sodium density unit is cm^{-3}.

of the Poisson distribution is calculated by averaging 120 consecutive raw profiles (i.e., 4 min). Thus, the statistical probability of photon counts can be calculated. In the altitude range of the regular sodium layer, events at which the signal in altitude channel I has a statistical probability of being less than 1×10^{-8} are registered as "potential trail events (PTEs)".

Then, we pick out meteor trails from these potential events using the following criteria: PTEs that occur in altitude channels I and I ± 1 within a window of 3 consecutive photon count profiles (6 s) are assumed to arise from a single meteor trail.

Three typical meteor trail events taken from lidar observational data are shown in Fig. 7. The meteor trail event in Fig. 7a occurred on 26 March 2017, from 23:57:31 local time to 23:57:39 and is visible in five consecutive 2-s density profiles. The maximum density appeared at 23:57:33, with an altitude of 86.09 km and a density of 14172 cm^{-3}. Fig. 7b and 7c are the other two meteor trail events that occurred on 15 April 2017 and 18 June 2017 with maximum densities of 25495 cm^{-3} and 63990 cm^{-3}, respectively.

3.3. Periodic variation analysis

The monthly average sodium density observed in 2017 is shown in Fig. 8a. The sodium layer mainly ranged from 85–95 km and was relatively strong in January, July and November, which is similar to the sodium density observed by the USTC narrowband sodium temperature and wind lidar from 2012–2016 [48]. According to previous sodium lidar research, long-term variations in the sodium layer show strong annual or semiannual characteristics [49–51]. Sodium column density (C_0), centroid height (Z_0) and RMS width (σ_0) in 2017 are fitted by annual plus semiannual fit, which is based on the minimum-mean-square-error fitting method:

$$\hat{x}(d) = A_0 + A_1 \cos[\frac{2\pi}{365}(d - d_1)] + A_2 \cos[\frac{4\pi}{365}(d - d_2)] \quad (1)$$

where A_0 is the annual average, A_1 and A_2 are the annual and semiannual amplitudes, respectively, and d_1 and d_2 are the annual and semiannual phases, respectively. The fitting results are shown in Table 2 and Figs. 8b–d. According to Table 2, the annual average column density was 2.60×10^9 cm^{-2}; the maximum annual and semiannual phases appeared on October 4, 2017 and February 22, 2017; the annual amplitude of the annual average was 24.69%, which is far greater than the semiannual amplitude to annual average ratio (5.75%). As shown in Fig. 8b, the maximum daily average column density was 5.12×10^9 cm^{-2}, which appeared on 8 November 2017. The minimum daily average column density was 1.44×10^9 cm^{-2}, which appeared on 25 May 2017. The fitting curve shows that the column density was gradually reduced from winter to summer and increased from summer to winter. Thus, the column density showed obvious annual variations.

Table 2
Annual plus semiannual fit of sodium layers in 2017.

	$C_0/(10^9$ $cm^{-2})$	Z_0/km	σ_0/km
A_0	2.60	90.93	3.96
A_1	0.64	0.26	0.08
A_2	0.15	0.48	0.37
d_1	351	307	264
d_2	125	136	14
A_1/A_0(%)	24.69	0.28	2.11
A_2/A_0 (%)	5.75	0.53	9.43

Centroid heights are shown in Fig. 8c. The maximum daily centroid height was 92.46 km, which appeared on 17 June 2017. The minimum daily centroid height was 89.21 km, which appeared on 7 June 2017. The average centroid height was 90.93 km, and the annual amplitude and semiannual amplitude to annual average ratio were 0.29% and 0.53%, respectively. The centroid heights over Hefei showed semiannual variations.

RMS widths are shown in Fig. 8d. The maximum daily RMS width was 5.59 km, which appeared on 13 January 2017; the minimum daily RMS width was 3.45 km, which appeared on 22 April 2017. The average RMS width was 3.96 km, and the annual amplitude and semiannual amplitude to annual average ratio were 2.11% and 9.43%, respectively. The RMS widths over Hefei showed semiannual variations.

In addition, the monthly average atmospheric temperature observations during 2017–2018 observed by the USTC Rayleigh and sodium lidar and the Sounding of the Atmosphere using Broadband Emission Radiometry (SABER) instrument are shown in Fig. 9. High temperatures appeared in the lidar observations in June and November in the range of 45–50 km, while high temperatures appeared in the SABER observations in May and June in the range of 45–50 km. The Rayleigh channel observation time in July is short; thus, the 65 km temperature data are missing.

3.4. Stratospheric aerosol observed over Hefei

Stratospheric aerosols determine a large quantity of chemical processes in the middle atmosphere, ozone layer, and thermal conditions of the Earth's surface. For example, spectral absorption and solar radiation scattering by aerosols can alter the planetary albedo of the Earth's atmospheric system, thus affecting the energy balance of the Earth–atmosphere system.

Stratospheric aerosols can be observed by the sodium channel of the lidar system. The extinction coefficient of stratospheric aerosols can be obtained according to the following equation:

$$\alpha_1(z) = -\frac{s_1}{s_2} \cdot \alpha_2(z) + \frac{X(z) \cdot \exp[-2(\frac{s_1}{s_2} - 1)\int_{z_c}^{z} \alpha_2(z')dz']}{\frac{X(z_c)}{\alpha_1(z_c) + \frac{s_1}{s_2} \cdot \alpha_2(z_c)} - 2\int_{z_c}^{z} X(z') \exp[-2(\frac{s_1}{s_2} - 1)\int_{z_c}^{z} \alpha_2(z'')dz'']dz'}, \quad (2)$$

where $\alpha_1(z)$ and $\alpha_2(z)$ represent extinction coefficients of aerosol particles and air molecules at altitude z, respectively; $\beta_1(z)$ and $\beta_2(z)$ represent backscatter coefficients of aerosol particles and air molecules at altitude z, respectively; $\beta_2(z)$ can be obtained through the international standard atmosphere model and molecular Rayleigh scattering theory; $s_1 = \alpha_1(z)/\beta_1(z)$ and $s_2 = \alpha_2(z)/\beta_2(z)$; s_1 is equal to 50 and s_2 is equal to $8\pi/3$; $X(z) = P(z)z^2$ and P(z) is the energy of the atmospheric backscattered echo signal at the height z; z_c is calibration height where $X(z)/\beta_z(z)$ is the minimum and $R(z_c) = 1 + \beta_1(z_c)/\beta_2(z_c) = 1.01$. During the lidar observations, a stratospheric aerosol was observed by the sodium channel for two consecutive days, i.e., 29 October 2017 and 30

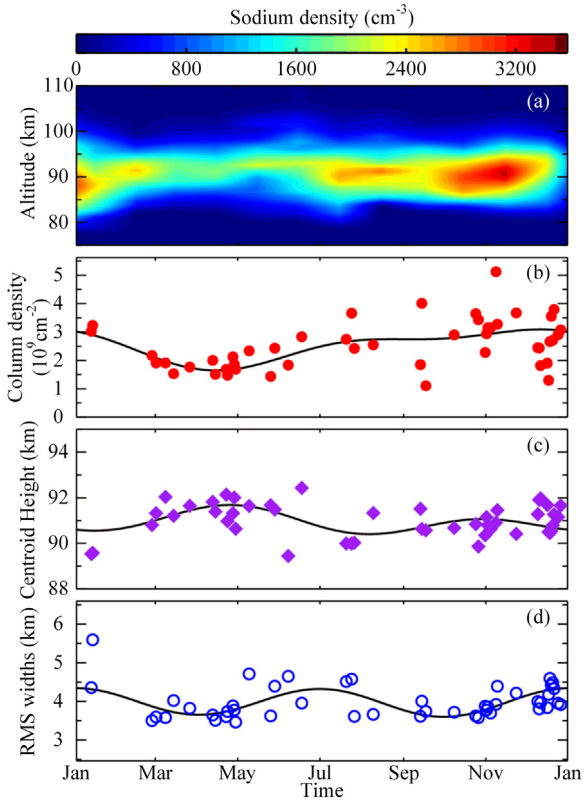

Fig. 8. Monthly average sodium density (a), sodium column density (b), centroid height (c) and RMS width (d) observed over Hefei during 2017.

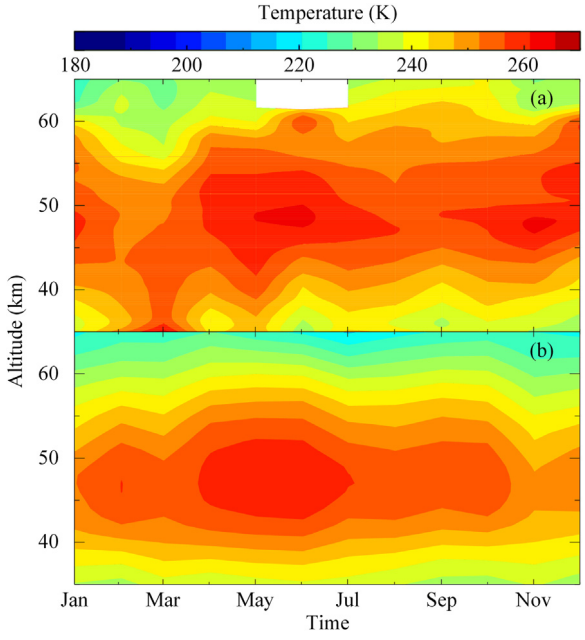

Fig. 9. Monthly average atmospheric temperature observed by USTC Rayleigh and sodium lidar during 2017–2018 (a) and SABER instrument during 2017–2018 (b).

October 2017, as shown in Fig. 10. This stratospheric aerosol showed a slight downward trend and ranged in altitude from 21 to 22 km. The observed aerosol layer may be caused by the atmospheric transport of forest fire products from the Lake Athabasca region (Saskatchewan and Alberta Provinces, Canada) to the atmosphere [52].

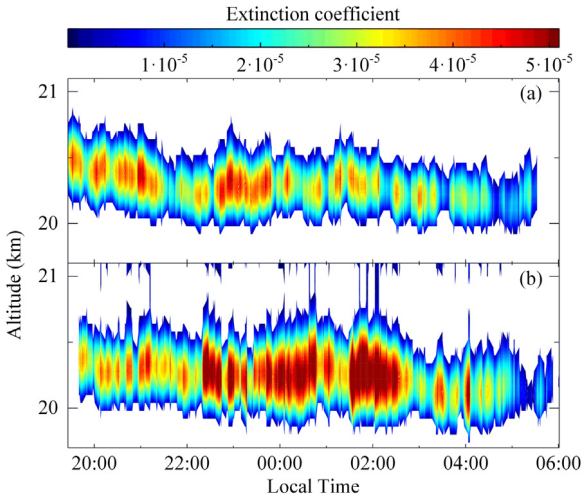

Fig. 10. Extinction coefficient observed by the sodium channel at night on 29 October 2017 (a) and 30 October 2017 (b), respectively.

4. Conclusion

A Rayleigh and sodium lidar system recently upgraded at the USTC in Hefei, China, was reported in this paper. The system combines Rayleigh backscatter and sodium scattering fluorescence channels. In this lidar system, an ND:YAG laser and a dye laser are used to generate two laser beams with wavelengths of 532 nm and 589 nm, respectively. A sodium cell is used in the lock unit to calibrate the wavelength of the 589 nm beam. A Cassegrain receiving telescope with a 1-meter diameter is used to receive the backscattering signals. The strong backscattering signals at low altitudes will be blocked by a chopper wheel with a diameter of 200 mm, which rotates at a rate of 6000 rpm. Then, signals will be divided in the wavelength-division multiplexing receiving system, and two channel signals will enter the same PMT, making the system compact and robust. Wideband filtering and narrowband filtering are both used in the lidar system to obtain high signal-to-noise ratio data under city lights. The entire lidar system is located in a square-shaped cabin, which makes the lidar system mobile.

The lidar system was established on 24 September 2016 and has run stably for 2 years. From the data that have been collected, the system has excellent resolutions and SNR. Atmospheric temperature, density and sodium density data observed on 20 July 2017 were shown. The Rayleigh signals can invert the atmospheric temperature and density up to over 70 km. An obvious sporadic sodium layer can be found in the sodium density observations. Meteor trail events that lasted for only a few seconds were extracted from the high resolution and high SNR observational data. The sodium observational data in 2017 were annual plus semiannual fitted to study the variations in the sodium layers. The column density showed obvious annual variations, while the centroid heights and RMS widths showed semiannual variations. The monthly average atmospheric temperature showed semiannual variations. Stratospheric aerosols were observed for two consecutive days during the observations, which may be due to the atmospheric transport of forest fire products.

Acknowledgments

This work is supported by the National Natural Science Foundation of China (41774158, 41674150, 41831071), the Open Research Project of Large Research Infrastructures of CAS, China - “Study on the interaction between low/mid-latitude atmosphere and ionosphere based on the Chinese Meridian Project”, the Youth Innovation Promotion

Association of the Chinese Academy of Sciences, China (2011324). In addition, thanks are due to Dr. Zhifeng Shu, Dr. Mingjiao Jia and Mr. Xiang Shang for their technological help.

References

[1] U. von Zahn, Are noctilucent clouds a "Miner's Canary" for global change?, EOS Trans. Am. Geophys. Union 84 (2003) 261, http://dx.doi.org/10.1029/2003eo280001.

[2] G.E. Thomas, J.J. Olivero, E.J. Jensen, W. Schroeder, O.B. Toon, Relation between increasing methane and the presence of ice clouds at the mesopause, Nature 338 (1989) 490–492, http://dx.doi.org/10.1038/338490a0.

[3] R.M. Cox, J.M.C. Plane, An ion-molecule mechanism for the formation of neutral sporadic Na layers, J. Geophys. Res.: Atmos. 103 (1998) 6349–6359, http://dx.doi.org/10.1029/97jd03376.

[4] J.D. Mathews, Sporadic E: current views and recent progress, J. Atmos. Sol.-Terr. Phys. 60 (1998) 413–435, http://dx.doi.org/10.1016/s1364-6826(97)00043-6.

[5] A. Hauchecorne, M.-L. Chanin, Density and temperature profiles obtained by lidar between 35 and 70 km, Geophys. Res. Lett. 7 (1980) 565–568, http://dx.doi.org/10.1029/GL007i008p00565.

[6] G.S. Kent, R.W.H. Wright, A review of laser radar measurements of atmospheric properties, J. Atmos. Terr. Phys. 32 (1970) 917–943, http://dx.doi.org/10.1016/0021-9169(70)90036-x.

[7] X. Dou, Y. Han, D. Sun, H. Xia, Z. Shu, R. Zhao, M. Shangguan, J. Guo, Mobile Rayleigh Doppler lidar for wind and temperature measurements in the stratosphere and lower mesosphere, Opt. Express 22 (Suppl 5) (2014) A1203–1221, http://dx.doi.org/10.1364/OE.22.0A1203.

[8] H. Xia, X. Dou, M. Shangguan, R. Zhao, D. Sun, C. Wang, J. Qiu, Z. Shu, X. Xue, Y. Han, Y. Han, Stratospheric temperature measurement with scanning Fabry–Perot interferometer for wind retrieval from mobile Rayleigh Doppler lidar, Opt. Express 22 (2014) 21775–21789, http://dx.doi.org/10.1364/OE.22.021775.

[9] H. Xia, X. Dou, D. Sun, Z. Shu, X. Xue, Y. Han, D. Hu, Y. Han, T. Cheng, Mid-altitude wind measurements with mobile Rayleigh Doppler lidar incorporating system-level optical frequency control method, Opt. Express 20 (2012) 15286–15300, http://dx.doi.org/10.1364/OE.20.015286.

[10] L. Sox, V.B. Wickwar, T. Yuan, N.R. Criddle, Simultaneous Rayleigh-scatter and sodium resonance lidar temperature comparisons in the mesosphere-lower thermosphere, J. Geophys. Res. Atmos. 123 (2018) 10688–10706, http://dx.doi.org/10.1029/2018jd029438.

[11] A. Jalali, R.J. Sica, A. Haefele, Improvements to a long-term Rayleigh-scatter lidar temperature climatology by using an optimal estimation method, Atmos. Meas. Tech. 11 (2018) 6043–6058, http://dx.doi.org/10.5194/amt-11-6043-2018.

[12] J. Xu, A.K. Smith, Perturbations of the sodium layer: controlled by chemistry or dynamics? Geophys. Res. Lett. 30 (2003) http://dx.doi.org/10.1029/2003gl018040.

[13] C.Y. She, S. Chen, Z. Hu, J. Sherman, J.D. Vance, V. Vasoli, M.A. White, J. Yu, D.A. Krueger, Eight-year climatology of nocturnal temperature and sodium density in the mesopause region (80 to 105 km) over Fort Collins, Co (41°N, 105°W), Geophys. Res. Lett. 27 (2000) 3289–3292, http://dx.doi.org/10.1029/2000gl003825.

[14] R. Delgado, J.S. Friedman, J.T. Fentzke, S. Raizada, C.A. Tepley, Q. Zhou, Sporadic metal atom and ion layers and their connection to chemistry and thermal structure in the mesopause region at Arecibo, J. Atmos. Sol.-Terr. Phys. 74 (2012) 11–23, http://dx.doi.org/10.1016/j.jastp.2011.09.004.

[15] B.R. Clemesha, V.W.J.H. Kirchhoff, D.M. Simonich, H. Takahashi, Evidence of an extra-terrestrial source for the mesospheric sodium layer, Geophys. Res. Lett. 5 (1978) 873–876, http://dx.doi.org/10.1029/GL005i010p00873.

[16] J.M.C. Plane, A time-resolved model of the mesospheric Na layer: constraints on the meteor input function, Atmos. Chem. Phys. 4 (2004) 627–638, http://dx.doi.org/10.5194/acp-4-627-2004.

[17] J.M.C. Plane, R.M. Cox, R.J. Rollason, Metallic layers in the mesopause and lower thermosphere region, Adv. Space Res. 24 (1999) 1559–1570, http://dx.doi.org/10.1016/s0273-1177(99)00880-7.

[18] D.A. Krueger, C.Y. She, T. Yuan, Retrieving mesopause temperature and line-of-sight wind from full-diurnal-cycle Na lidar observations, Appl. Opt. 54 (2015) 9469–9489, http://dx.doi.org/10.1364/ao.54.009469.

[19] B.R. Clemesha, D.M. Simonich, P.P. Batista, H. Takahashi, Seasonal variation in the solar diurnal tide and its possible influence on the atmospheric sodium layer, Adv. Space Res. 35 (2005) 1951–1956, http://dx.doi.org/10.1016/j.asr.2005.02.081.

[20] C.S. Gardner, Seasonal variations of the Na and Fe layers at the South Pole and their implications for the chemistry and general circulation of the polar mesosphere, J. Geophys. Res. 110 (2005) http://dx.doi.org/10.1029/2004jd005670.

[21] T. Yuan, C.Y. She, T.D. Kawahara, D.A. Krueger, Seasonal variations of midlatitude mesospheric na layer and their tidal period perturbations based on full diurnal cycle Na lidar observations of 2002–2008, J. Geophys. Res. Atmos. 117 (2012) 13, http://dx.doi.org/10.1029/2011jd017031.

[22] C. Nagasawa, M. Abo, Lidar observations of a lot of sporadic sodium layers in mid-latitude, Geophys. Res. Lett. 22 (1995) 263–266, http://dx.doi.org/10.1029/94gl03008.

[23] T.T. Tsuda, S. Nozawa, T.D. Kawahara, T. Kawabata, N. Saito, S. Wada, C.M. Hall, M. Tsutsumi, Y. Ogawa, S. Oyama, T. Takahashi, M.K. Ejiri, T. Nishiyama, T. Nakamura, A. Brekke, A sporadic sodium layer event detected with five-directional lidar and simultaneous wind, electron density, and electric field observation at Tromsø, Norway, Geophys. Res. Lett. 42 (2015) 9190–9196, http://dx.doi.org/10.1002/2015gl066411.

[24] S.S. Gong, G.T. Yang, J.M. Wang, B.M. Liu, X.W. Cheng, J.Y. Xu, W.X. Wan, Occurrence and characteristics of sporadic sodium layer observed by lidar at a mid-latitude location, J. Atmos. Sol.-Terr. Phys. 64 (2002) 1957–1966, http://dx.doi.org/10.1016/s1364-6826(02)00216-x.

[25] J. Qian, Y. Gu, C.S. Gardner, Characteristics of the sporadic Na layers observed during the airborne lidar and observations of Hawaiian airglow/airborne noctilucent cloud (ALOHA/ANLC-93) campaigns, J. Geophys. Res.: Atmos. 103 (1998) 6333–6347, http://dx.doi.org/10.1029/97jd03374.

[26] B. Yu, X. Xue, G. Lu, C.-L. Kuo, X. Dou, Q. Gao, X. Qie, J. Wu, S. Qiu, Y. Chi, Y. Tang, The enhancement of neutral metal Na layer above thunderstorms, Geophys. Res. Lett. 44 (2017) 9555–9563, http://dx.doi.org/10.1002/2017gl074977.

[27] F. Yi, S. Zhang, C. Yu, Y. He, X. Yue, C. Huang, J. Zhou, Simultaneous observations of sporadic Fe and Na layers by two closely colocated resonance fluorescence lidars at Wuhan (30.5°N, 114.4°E), China, J. Geophys. Res. 112 (2007) http://dx.doi.org/10.1029/2006jd007413.

[28] X.H. Xue, X.K. Dou, J. Lei, J.S. Chen, Z.H. Ding, T. Li, Q. Gao, W.W. Tang, X.W. Cheng, K. Wei, Lower thermospheric-enhanced sodium layers observed at low latitude and possible formation: Case studies, J. Geophys. Res. Space Phys. 118 (2013) 2409–2418, http://dx.doi.org/10.1002/jgra.50200.

[29] X.K. Dou, S.C. Qiu, X.H. Xue, T.D. Chen, B.Q. Ning, Sporadic and thermospheric enhanced sodium layers observed by a lidar chain over China, J. Geophys. Res. Space Phys. 118 (2013) 6627–6643, http://dx.doi.org/10.1002/jgra.50579.

[30] J.H. Wang, Y. Yang, X.W. Cheng, G.T. Yang, S.L. Song, S.S. Gong, Double sodium layers observation over Beijing, China, Geophys. Res. Lett. 39 (2012) http://dx.doi.org/10.1029/2012gl052134.

[31] S.S. Gong, G.T. Yang, J.M. Wang, X.W. Cheng, F.Q. Li, W.X. Wan, A double sodium layer event observed over Wuhan, China by lidar, Geophys. Res. Lett. 30 (2003) http://dx.doi.org/10.1029/2002gl016135.

[32] Q. Gao, X. Chu, X. Xue, X. Dou, T. Chen, J. Chen, Lidar observations of thermospheric Na layers up to 170 km with a descending tidal phase at Lijiang (26.7°N, 100.0°E), China, J. Geophys. Res. Space Phys. 120 (2015) 9213–9220, http://dx.doi.org/10.1002/2015ja021808.

[33] X. Chu, A.Z. Liu, G. Papen, C.S. Gardner, M. Kelley, J. Drummond, R. Fugate, Lidar observations of elevated temperatures in bright chemiluminescent meteor trails during the 1998 leonid shower, Geophys. Res. Lett. 27 (2000) 1815–1818, http://dx.doi.org/10.1029/2000gl000080.

[34] Y.J. Liu, J.M.C. Plane, B.R. Clemesha, J.H. Wang, X.W. Cheng, Meteor trail characteristics observed by high time resolution lidar, Ann. Geophys. 32 (2014) 1321–1332, http://dx.doi.org/10.5194/angeo-32-1321-2014.

[35] C. Ban, T. Li, X. Fang, X. Dou, J. Xiong, Sodium lidar-observed gravity wave breaking followed by an upward propagation of sporadic sodium layer over Hefei, China, J. Geophys. Res. Space Phys. 120 (2015) 7958–7969, http://dx.doi.org/10.1002/2015ja021339.

[36] C.S. Gardner, D.G. Voelz, Lidar studies of the nighttime sodium layer over Urbana, Illinois: 2. Gravity waves, J. Geophys. Res. 92 (1987) 4673, http://dx.doi.org/10.1029/JA092iA05p04673.

[37] X. Lu, A.Z. Liu, G.R. Swenson, T. Li, T. Leblanc, I.S. McDermid, Gravity wave propagation and dissipation from the stratosphere to the lower thermosphere, J. Geophys. Res. 114 (2009) http://dx.doi.org/10.1029/2008jd010112.

[38] J. Hildebrand, G. Baumgarten, J. Fiedler, U.P. Hoppe, B. Kaifler, F.J. Lübken, B.P. Williams, Combined wind measurements by two different lidar instruments in the Arctic middle atmosphere, Atmos. Meas. Tech. 5 (2012) 2433–2445, http://dx.doi.org/10.5194/amt-5-2433-2012.

[39] D.C. Fritts, R.B. Smith, M.J. Taylor, J.D. Doyle, S.D. Eckermann, A. Dörnbrack, M. Rapp, B.P. Williams, P.D. Pautet, K. Bossert, N.R. Criddle, C.A. Reynolds, P.A. Reinecke, M. Uddstrom, M.J. Revell, R. Turner, B. Kaifler, J.S. Wagner, T. Mixa, C.G. Kruse, A.D. Nugent, C.D. Watson, S. Gisinger, S.M. Smith, R.S. Lieberman, B. Laughman, J.J. Moore, W.O. Brown, J.A. Haggerty, A. Rockwell, G.J. Stossmeister, S.F. Williams, G. Hernandez, D.J. Murphy, A.R. Klekociuk, I.M. Reid, J. Ma, The deep propagating gravity wave experiment (DEEPWAVE): An airborne and ground-based exploration of gravity wave propagation and effects from their sources throughout the lower and middle atmosphere, Bull. Am. Meteorol. Soc. 97 (2016) 425–453, http://dx.doi.org/10.1175/bams-d-14-00269.1.

[40] X. Fang, T. Li, C. Ban, Z. Wu, J. Li, F. Li, Y. Cen, B. Tian, A mobile differential absorption lidar for simultaneous observations of tropospheric and stratospheric ozone over Tibet, Opt. Express 27 (2019) 4126, http://dx.doi.org/10.1364/oe.27.004126.

[41] K.S. Arnold, C.Y. She, Metal fluorescence lidar (light detection and ranging) and the middle atmosphere, Contemp. Phys. 44 (2003) 35–49, http://dx.doi.org/10.1080/00107510302713.

[42] T. Li, X. Fang, W. Liu, S.Y. Gu, X. Dou, Narrowband sodium lidar for the measurements of mesopause region temperature and wind, Appl. Opt. 51 (2012) 5401–5411, http://dx.doi.org/10.1364/AO.51.005401.
[43] L. Zeng, F. Yi, Lidar observations of Fe and Na meteor trails with high temporal resolution, J. Atmos. Sol.-Terr. Phys. 73 (2011) 2367–2372, http://dx.doi.org/10.1016/j.jastp.2011.08.002.
[44] T.J. Kane, C.S. Gardner, Q. Znou, J.D. Mathews, C.A. Tepley, Lidar, radar and airglow observations of a prominent sporadic Na/sporadic E layer event at Arecibo during AIDA-89, J. Atmos. Terr. Phys. 55 (1993) 499–511, http://dx.doi.org/10.1016/0021-9169(93)90084-c.
[45] T.J. Kane, C.S. Gardner, Lidar observations of the meteoric deposition of mesospheric metals, Science 259 (1993) 1297–1300, http://dx.doi.org/10.1126/science.259.5099.1297.
[46] T. Pfrommer, P. Hickson, C.-Y. She, A large-aperture sodium fluorescence lidar with very high resolution for mesopause dynamics and adaptive optics studies, Geophys. Res. Lett. 36 (2009) http://dx.doi.org/10.1029/2009gl038802.
[47] Q. Xie, F. Yi, Preliminary lidar observations of Na meteor trails at Wuhan (30.5°N, 114.4°E), China, Chin. Sci. Bull. 55 (2010) 2422–2427, http://dx.doi.org/10.1007/s11434-010-3018-6.
[48] T. Li, C. Ban, X. Fang, J. Li, Z. Wu, W. Feng, J.M.C. Plane, J. Xiong, D.R. Marsh, M.J. Mills, X. Dou, Climatology of mesopause region nocturnal temperature, zonal wind and sodium density observed by sodium lidar over Hefei, China (32°N, 117°E), Atmos. Chem. Phys. 18 (2018) 11683–11695, http://dx.doi.org/10.5194/acp-18-11683-2018.
[49] B.R. Clemesha, P.P. Batista, D.M. Simonich, Long-term variations in the centroid height of the atmospheric sodium layer, Adv. Space Res. 32 (2003) 1707–1711, http://dx.doi.org/10.1016/s0273-1177(03)90466-2.
[50] C.S. Gardner, D.G. Voelz, C.F. Sechrist, A.C. Segal, Lidar studies of the nighttime sodium layer over Urbana, Illinois: 1. Seasonal and nocturnal variations, J. Geophys. Res. 91 (1986) 13659, http://dx.doi.org/10.1029/JA091iA12p13659.
[51] R.J. States, C.S. Gardner, Structure of the mesospheric Na layer at 40 degrees N latitude: Seasonal and diurnal variations, J. Geophys. Res. Atmos. 104 (1999) 11783–11798, http://dx.doi.org/10.1029/1999jd900002.
[52] M. Haarig, A. Ansmann, H. Baars, C. Jimenez, I. Veselovskii, R. Engelmann, D. Althausen, Depolarization and lidar ratios at 355, 532, and 1064 nm and microphysical properties of aged tropospheric and stratospheric Canadian wildfire smoke, Atmos. Chem. Phys. 18 (2018) 11847–11861, http://dx.doi.org/10.5194/acp-18-11847-2018.